Supplementary Information

Surface evolution of Zn doped-RuO_2 under different etching methods towards acidic oxygen evolution

Ya-Nan Zhou, Ning Yu, Qian-Xi Lv, Bin Liu, Bin Dong *, Yong-Ming Chai *

State Key Laboratory of Heavy Oil Processing, College of Chemistry and Chemical Engineering,

China University of Petroleum (East China), Qingdao 266580, PR China

* Corresponding author. Email: dongbin@upc.edu.cn (B. Dong); ymchai@upc.edu.cn (Y.M. Chai)

Tel: +86-532-86981156, Fax: +86-532-86981156

Characterization

The morphologies and microstructure of all samples were characterized using SEM (JEM 2100F) and TEM (FEI Tecni G20, 200 kV). X-ray diffraction (XRD) with Cu Kα radiation (λ = 1.54 Å) using the Brook D8 advance equipment to examine the crystalline structures and phase purity of the samples. Raman spectrum was obtained via LabRAM HR Evolution with an excitation wavelength of 514 nm. The element composition of the sample were characterized by the inductively coupled plasma mass spectrometry (ICP-MS) detected on the Agilent ICPMS7700. X-ray photoelectron spectroscopy (XPS) was acquired on Thermo Fisher K-alpha 250Xi to quantitatively research the chemical and electronic states of the sample elements.

Electrochemical measurements

Electrochemical tests were performed at room temperature on a standard three-electrode configuration in 0.5 M H_2SO_4 with Gamry Reference 3000 electrochemical equipment. The working electrode was prepared as follows: 5 mg catalyst and 20 μL Nafion solution (5 wt %) were dispersed in 1 mL of water/ethanol solution (v_{water} : $v_{ethanol}$ = 1:1) by sonicating at least 30 min to form a homogeneous ink. Then 5 μL of suspensions were coated on glassy carbon electrode (GCE) with a diameter of 3 mm, and dried in air before measurement. The glassy carbon (GC) electrode loaded catalyst, platinum electrode and saturated calomel electrode (SCE) were used as working electrode, counter electrode and reference electrode, respectively. The linear sweep voltammetry (LSV) were detected at same condition with scan rate of 5 mV s^{-1} with iR-correction. All the potentials vs. SCE were converted into a standard reversible hydrogen electrode (RHE) via the Nernst equation: $E_{RHE} = E_{SCE} + 0.0594\ pH + 0.245$. The

electrical double-layer capacitances (C_{dl}) were calculated by cyclic voltammetry (CV) curves with the scan rate of 40, 60, 80, 100, 120 mV s^{-1}, respectively. And electrochemical impedance spectroscopy (EIS) was performed with the frequency ranges from 10^5 Hz to 0.1 Hz. The stability of the samples was measured through CV curves for 2000 cycles at 40 mV s^{-1} and chronopotentiometry at constant current density of 10 mA cm^{-2}.

Estimation of turnover frequencies

The calculations used to determine the TOF values are shown below, taking RuO_2 as an example. The density was calculated using the crystal structure (unit cell) of RuO_2. Theoretical surface area values were obtained by assuming that a 0.5 nm shell represents the surface of a solid 5 nm particle. Turnover frequencies were estimated per surface atom (Ru and O) rather than per oxygen binding site, because the oxygen-binding sites can not be explicitly known.

Volume: 64.804 $Å^3$

Density: 6.82 g cm^{-3}

Volume of a 5 nm sphere: 5.236×10^{-19} cm^3

Surface area of a 5 nm sphere: 3.142×10^{-12} cm^2

Current density at some certain overpotential (mV) is obtained from LSVs of RuO_2: I, A cm^{-2}.

Active sites per real surface area:

$$\left(\frac{11\ atoms/unit\ cell}{64.804\ Å^3/unit\ cell}\right)^{2}/_{3} = 3.066\ \times 10^{15}\ \frac{atoms}{cm^2}$$

Surface area per gram of 5 nm sphere:

$$\frac{3.142 \times 10^{-12}\, cm^2}{1\, particle} \times \frac{1\, particle}{5.236 \times 10^{-19} cm^3} \times \frac{1\, cm^3}{6.82\, g} = 879.877 \frac{cm^2}{mg}$$

Surface atoms per testing area:

$$\frac{1\, mg}{50\, cm^2} \times \frac{879.877\, cm^2 (particle)}{mg} \times \frac{3.066 \times 10^{15}\, atoms}{1\, cm^2\, (particle)} = 5.395 \times 10^{16} \frac{cm^2}{mg}$$

Turnover frequency (per surface atom) with current density of I (A cm^{-2}) can be calculated by the following equation:

$$\frac{1\, turnoveer}{4\, e^-} \times \frac{I}{1\, cm^2} \times \frac{1\, mol}{96485\, C} \times \frac{6.022 \times 10^{23}\, e^-}{1\, mol} \times \frac{1\, test}{5.395 \times 10^{16}\, atoms} = 28.922\, I\, S^{-1}$$

DFT calculation

Density functional theory (DFT) calculations was performed using generalized gradient approximation (GGA) in the form of Perdew-Burke-Ernzerhof (PBE) for the exchange-correlation potentials [1,2], as implemented in the Material Studio. The OTFG ultrasoft pseudopotentials was used to describe the interaction between atomic cores and valence electrons with DFT. The optimized lattice constants of RuO_2 (110) and Zn-RuO_2 (110) are a=6.280 Å, b=6.425 Å, c=27.660 Å, respectively. Five-layered RuO_2 (110) slab model was employed to simulate the interaction surface. Moreover, based on the above RuO_2 (110) slab model, the model of Zn-RuO_2 (110) was built. In all of the slab structure optimization calculations, the bottom three layers was fixed, while the other atoms were fully relaxed until the residual force on each atom less than 0.03 eV $Å^{-1}$. The vacuum layers of these slab models are set to 20 Å in the z-direction for avoiding interaction between planes. The surface Brillouin-zone of RuO_2 (110) and Zn-RuO_2 (110) were sampled with k-meshes of 2×5×1 and 2×5×1, respectively. The transition states are searched by employing complete linear

synchronous transit (LST)/quadratic synchronous transit (QST) method. Furthermore, the force convergence tolerance on each atom in search of the minimum energy path was set to be 0.05 eV $Å^{-1}$. The free energies of the intermediates at 298 K were obtained using $\Delta G=\Delta E+\Delta ZPE-T\Delta S+eU$ according to previous work, where ΔE is the binding energy of adsorption species OH*, O* and OOH*, ΔZPE, ΔS and U are the zero point energy changes, entropy changes and applied potentials, respectively [3,4].

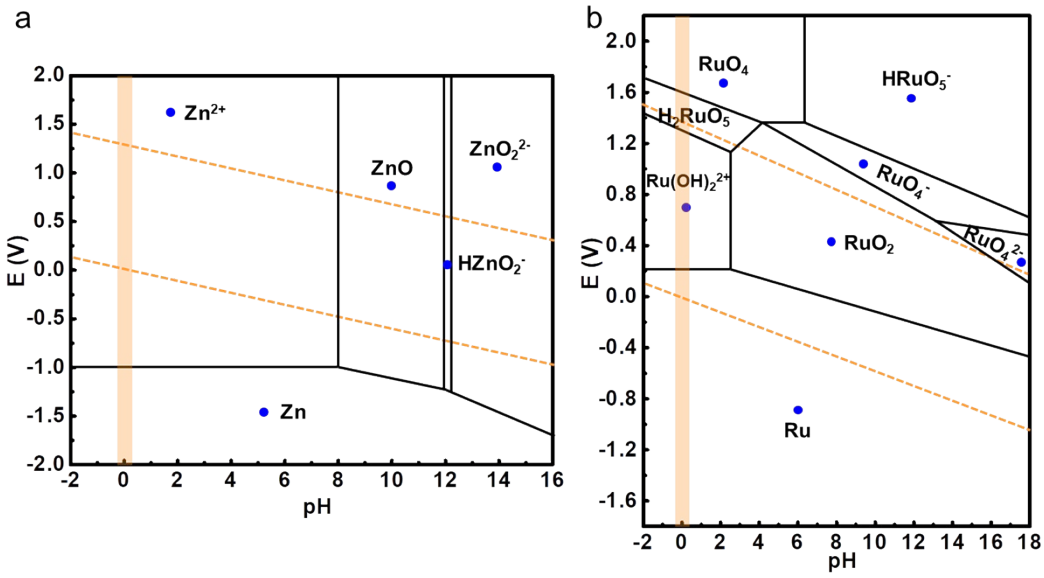

Fig. S1. Pourbaix diagram of (a) Ru and (c) Zn in aqueous solution.

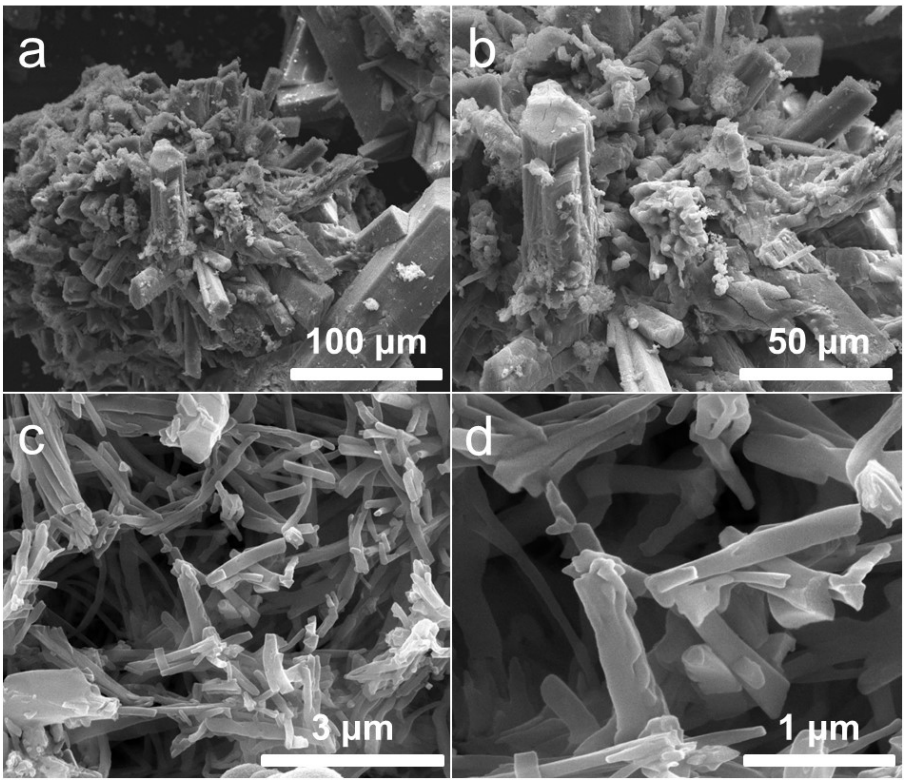

Fig. S2. SEM images of Zn-BTC (a,b) and Zn@C (c,d).

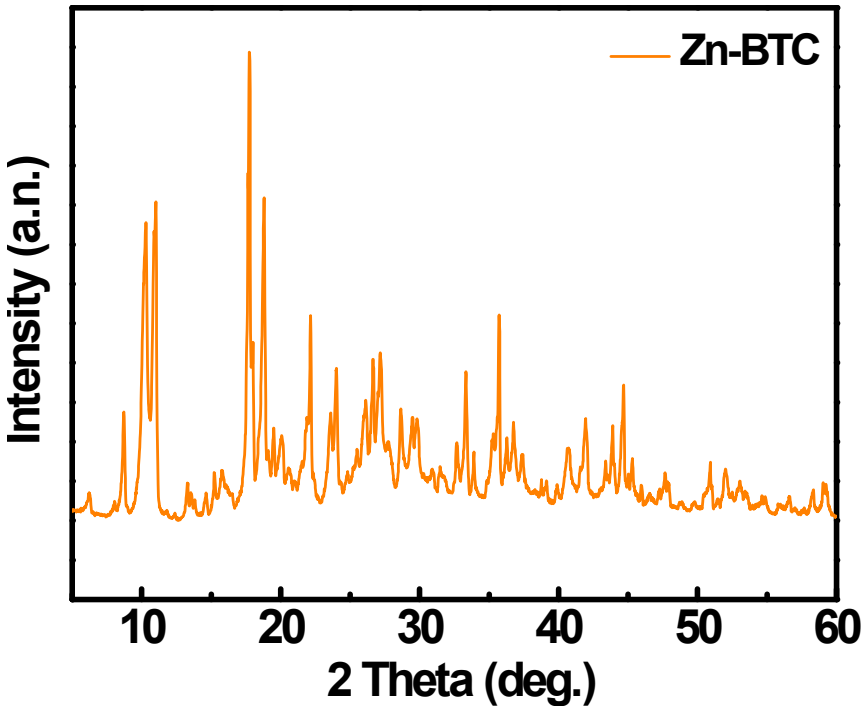

Fig. S3. XRD patterns of Zn-BTC precursor.

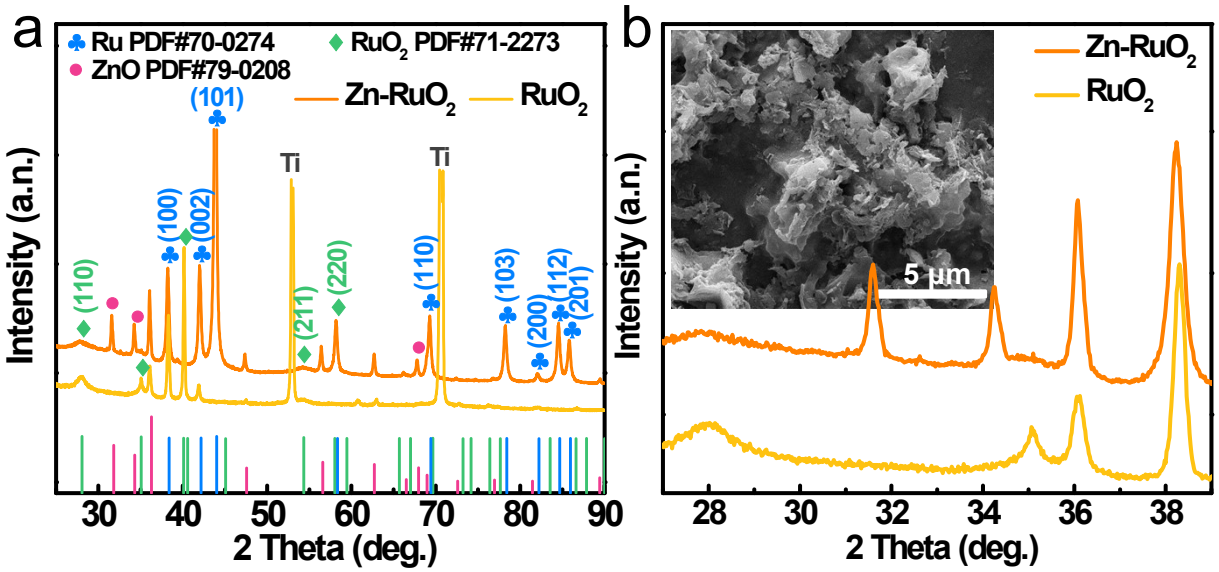

Fig. S4. XRD patterns of (a) RuO_2 and Zn-RuO_2 and (b) the enlarged XRD from 27° to 39°.

The insert is the morphologies of RuO_2 supported on Ti foil.

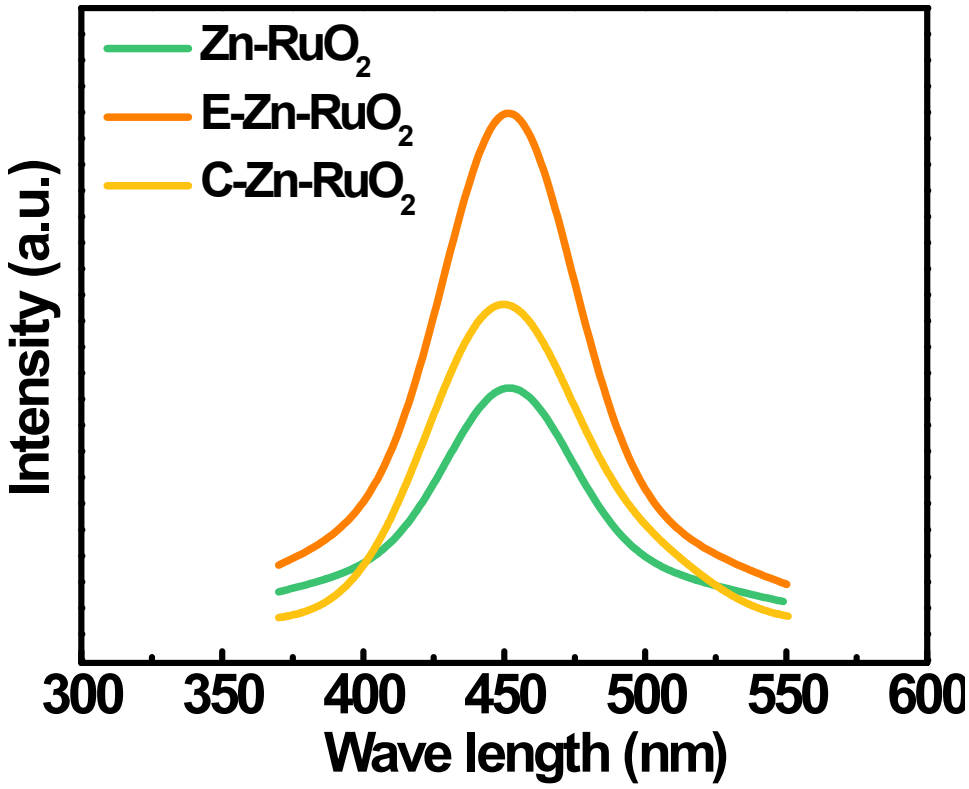

Fig. S5. PL signals of vacancy defects for Zn-RuO_2, E-Zn-RuO_2 and C-Zn-RuO_2.

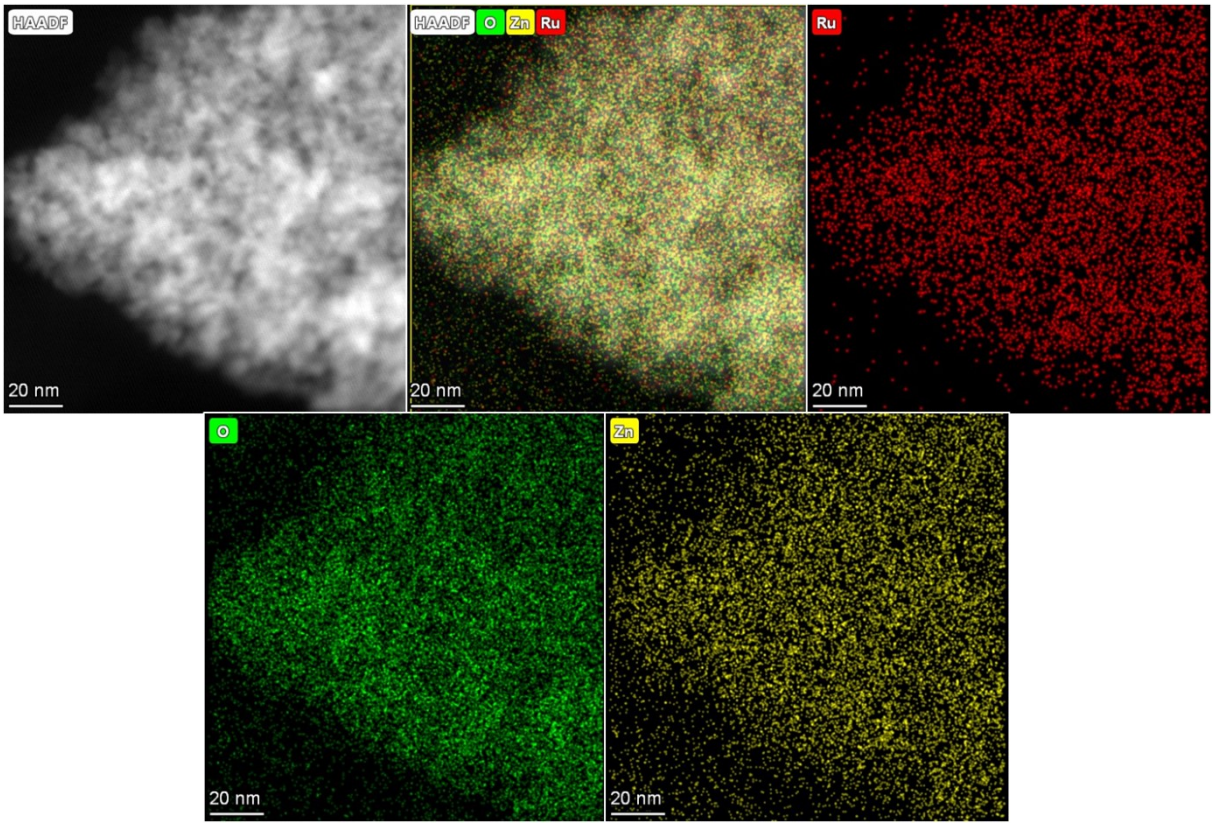

Fig. S6. Element mappings of Ru, O, Zn in Zn-RuO_2 sample.

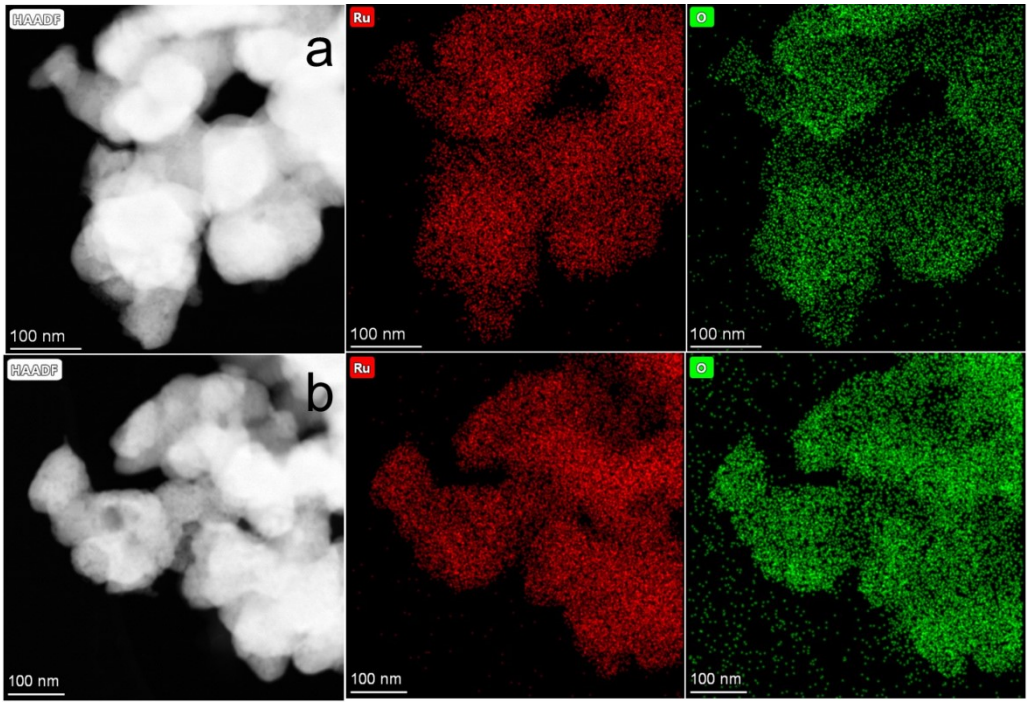

Fig. S7. Element mappings of Ru and O elements in (a) E-Zn-RuO_2 and (b) C-Zn-RuO_2 samples.

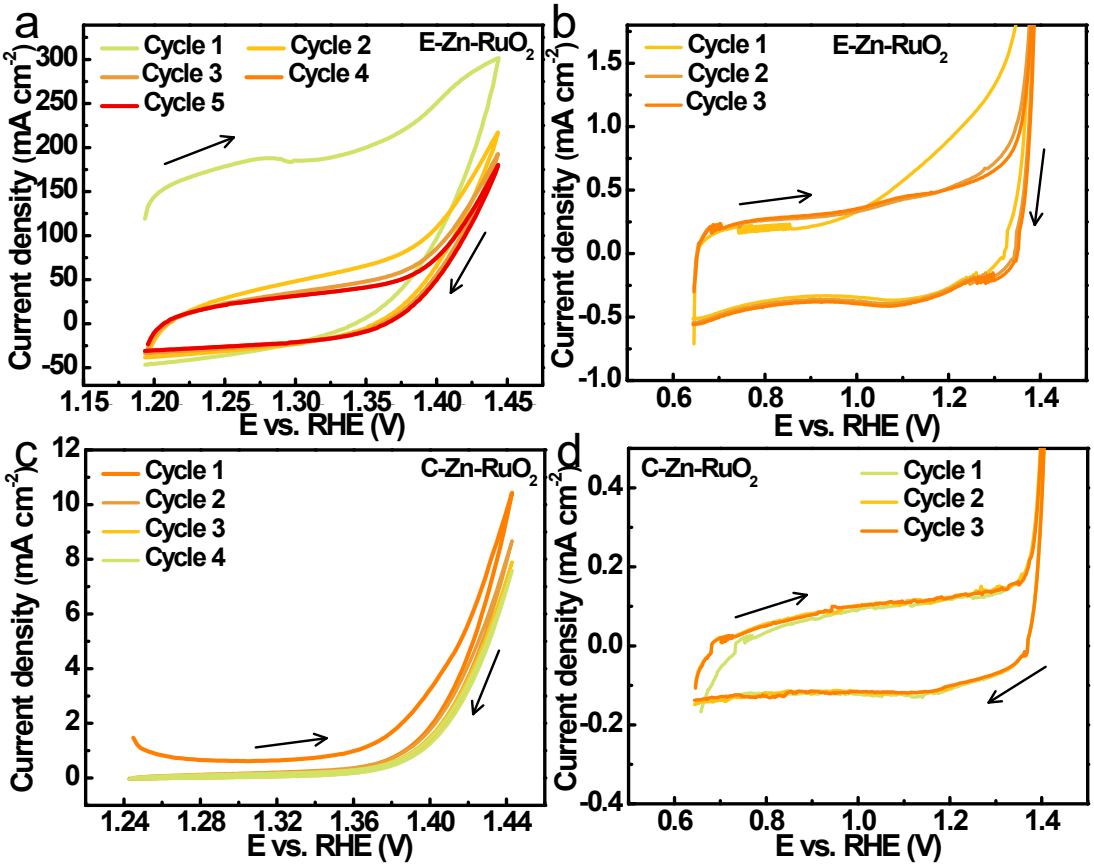

Fig. S8. Cycling CV curves of (a,b) E-Zn-RuO_2 and (c,d) C-Zn-RuO_2 samples in 0.5 M H_2SO_4 (scan rate: 10 mV s^{-1}).

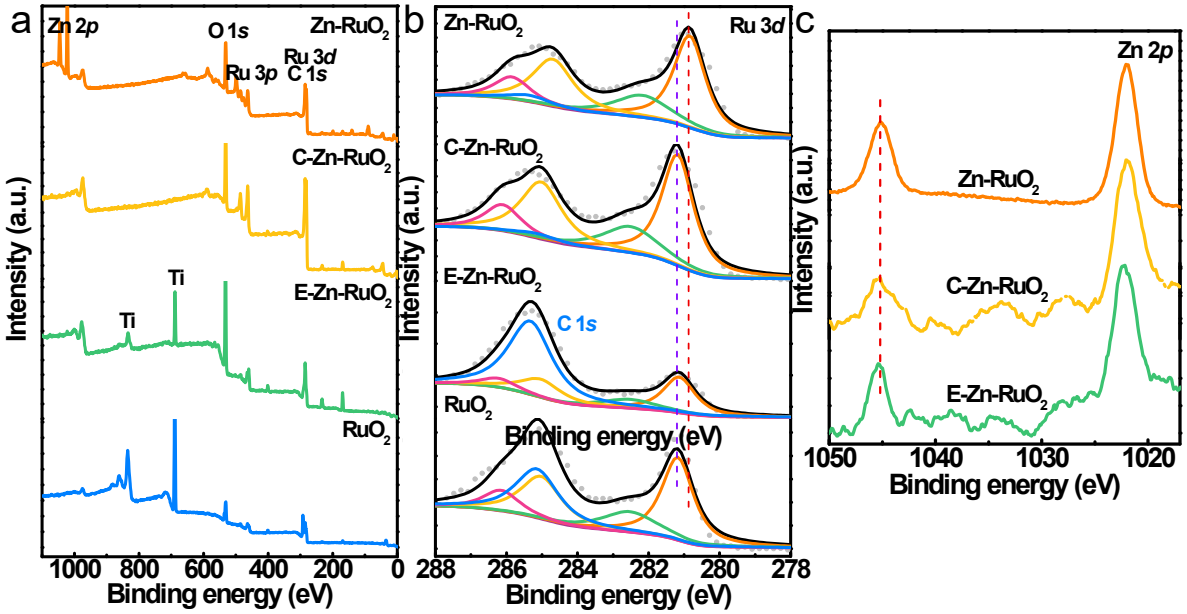

Fig. S9. High-resolution XPS of RuO_2, Zn-RuO_2, E-Zn-RuO_2 and C-Zn-RuO_2. (a) Overall survey scan, (b) Ru 3*d*, (c) Zn 2*p*.

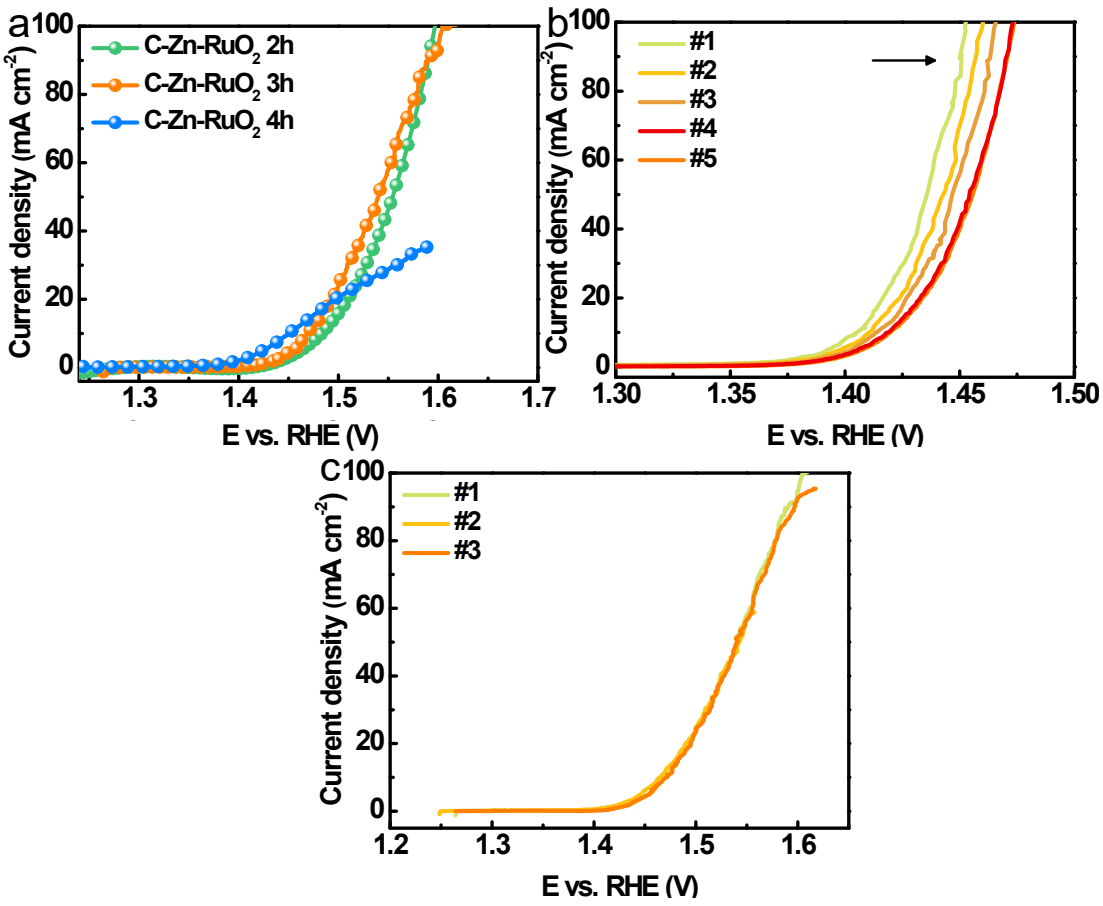

Fig. S10. (a) OER activity of C-Zn-RuO_2 2h, C-Zn-RuO_2 3h and C-Zn-RuO_2 4h. LSV scan process of E-Zn-RuO_2 (b) and C-Zn-RuO_2 (d).

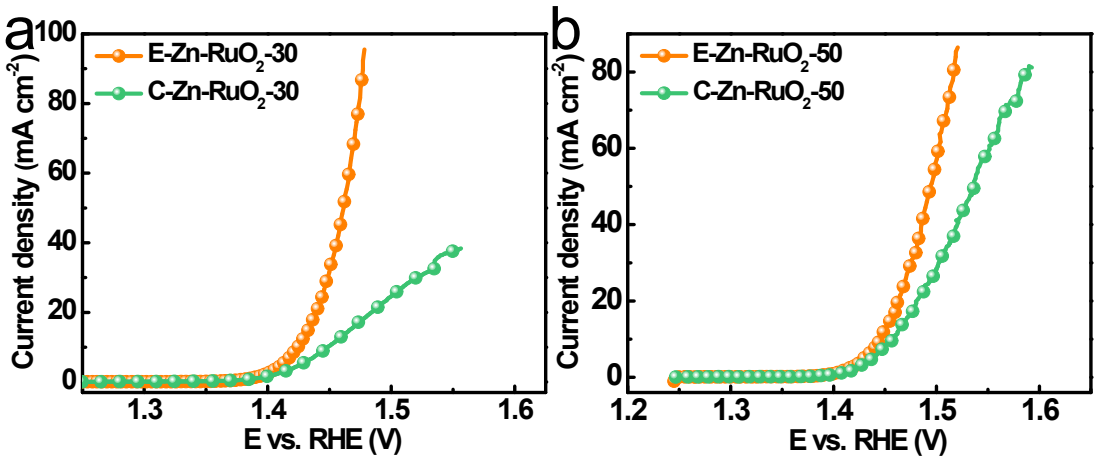

Fig. S11. OER activity of E-Zn-RuO_2-30 (a) and E-Zn-RuO_2-50 (b).

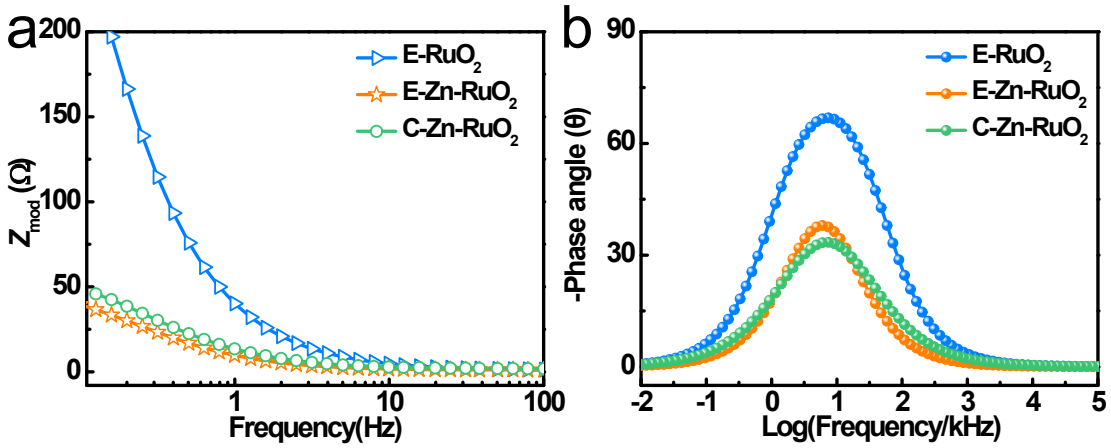

Fig. S12. Bode phase plots of pure E-RuO_2, E-Zn-RuO_2 and C-Zn-RuO_2 at 1.392 V vs. RHE in 1 M H_2SO_4.

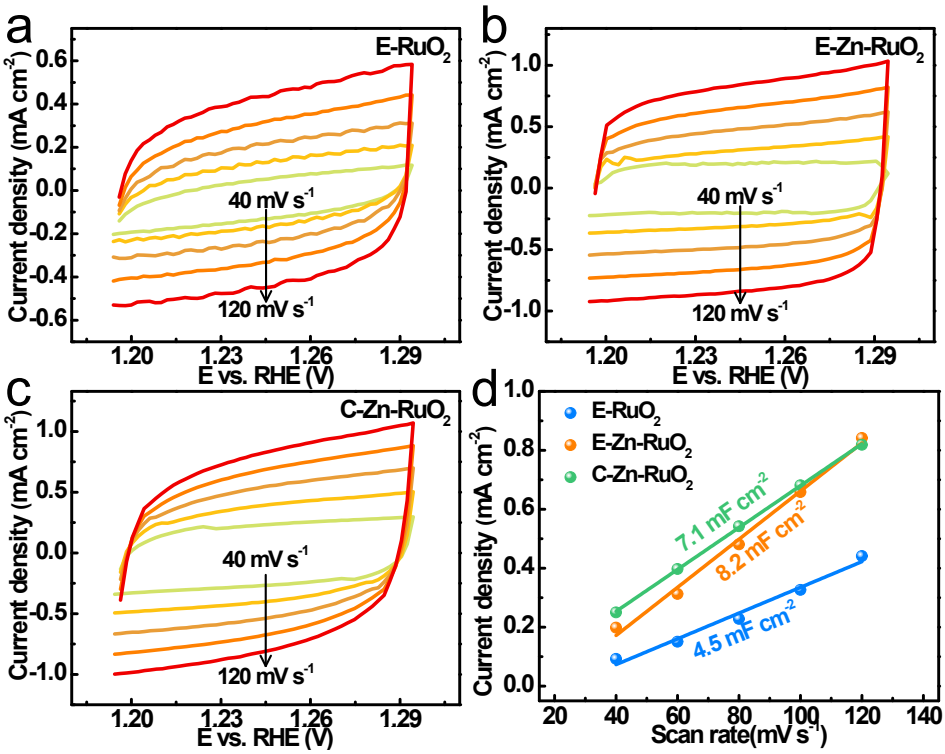

Fig. S13. CV curves of (a) E-RuO_2, (b) E-Zn-RuO_2 and (c) C-Zn-RuO_2 with the scan rate of 40, 60, 80, 100 and 120 mV s^{-1}. (d) C_{dl} plots of the three samples calculated from CVs at 1.245 V vs. RHE.

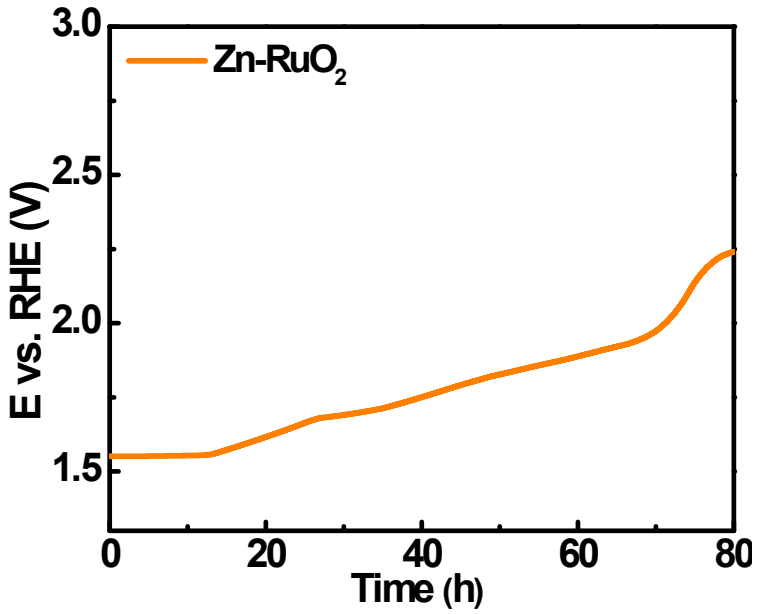

Fig. S14. *V-t* curves of pristine Zn-RuO_2 at 10 mA cm^{-2} in 0.5 M H_2SO_4.

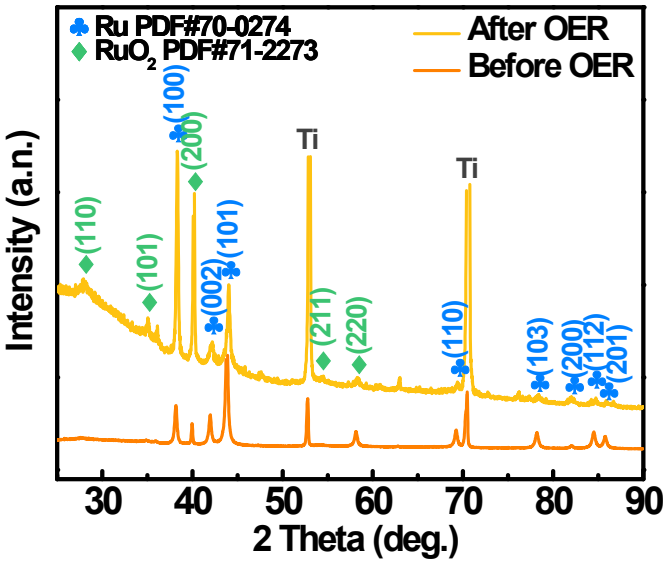

Fig. S15. XRD patterns of E-Zn-RuO_2 before and after acidic OER stability test for over 60 h.

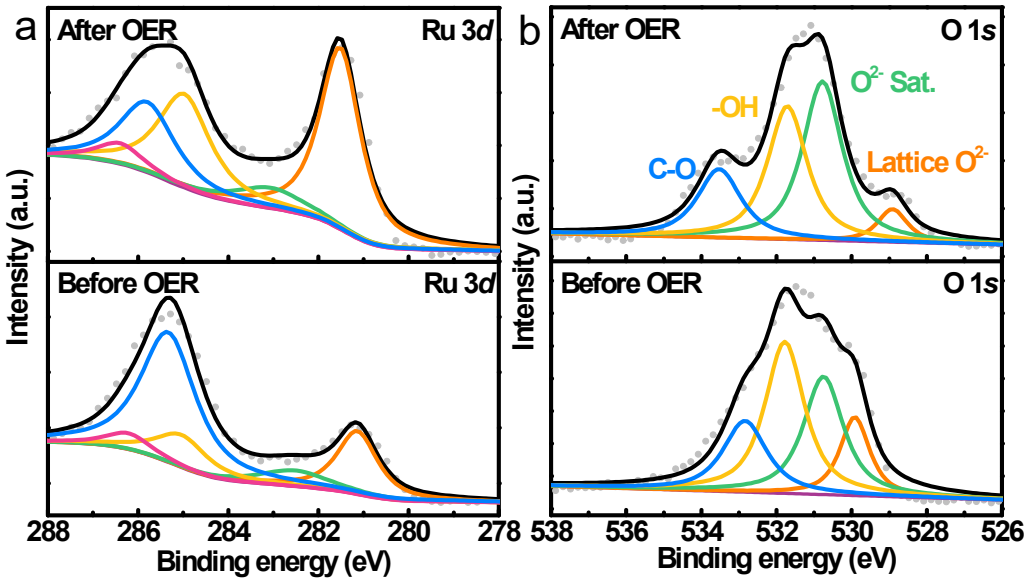

Fig. S16. XPS of (a) Ru 3*d* and (b) O 1*s* of E-Zn-RuO_2 before and after acidic OER stability test for over 60 h.

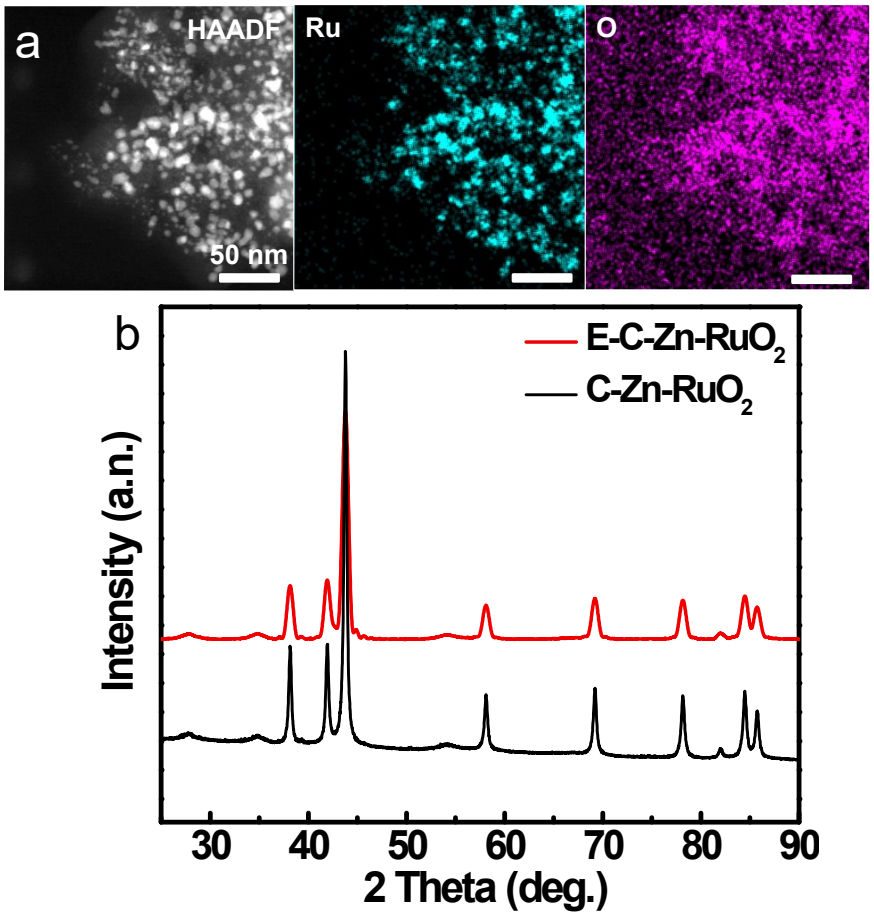

Fig. S17. (a) Element mapping and (b) XRD of C-Zn-RuO_2 after electrochemical etching (E-C-Zn-RuO_2).

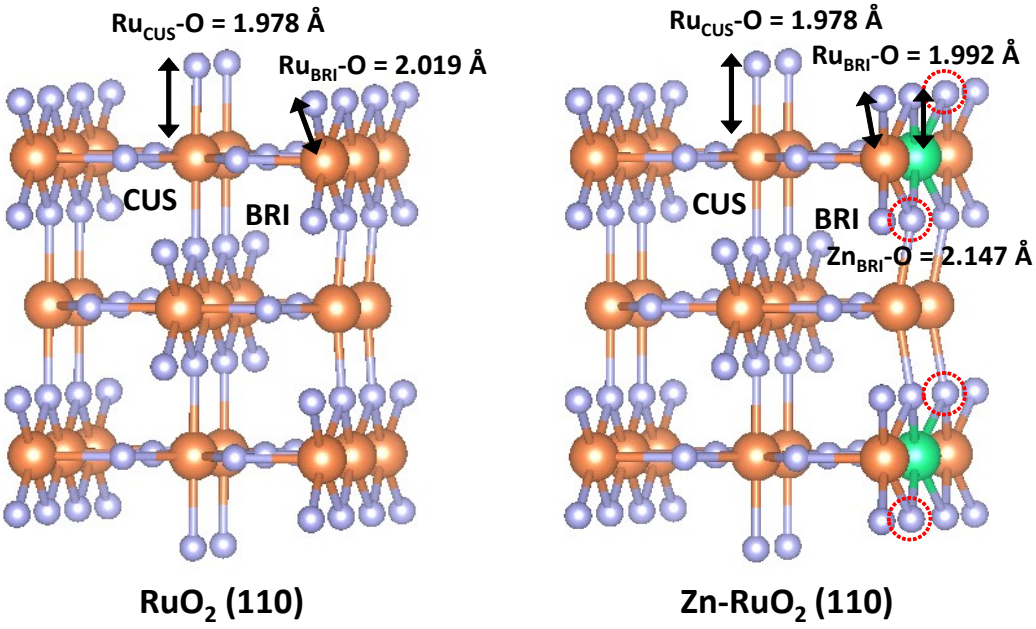

Fig. S18. Ball and stick models for the RuO_2 (110) and Zn-RuO_2 (110) structures obtained from the crystal truncation rod data. Orange, green and purple spheres represent Ru, Zn and O atoms, respectively.

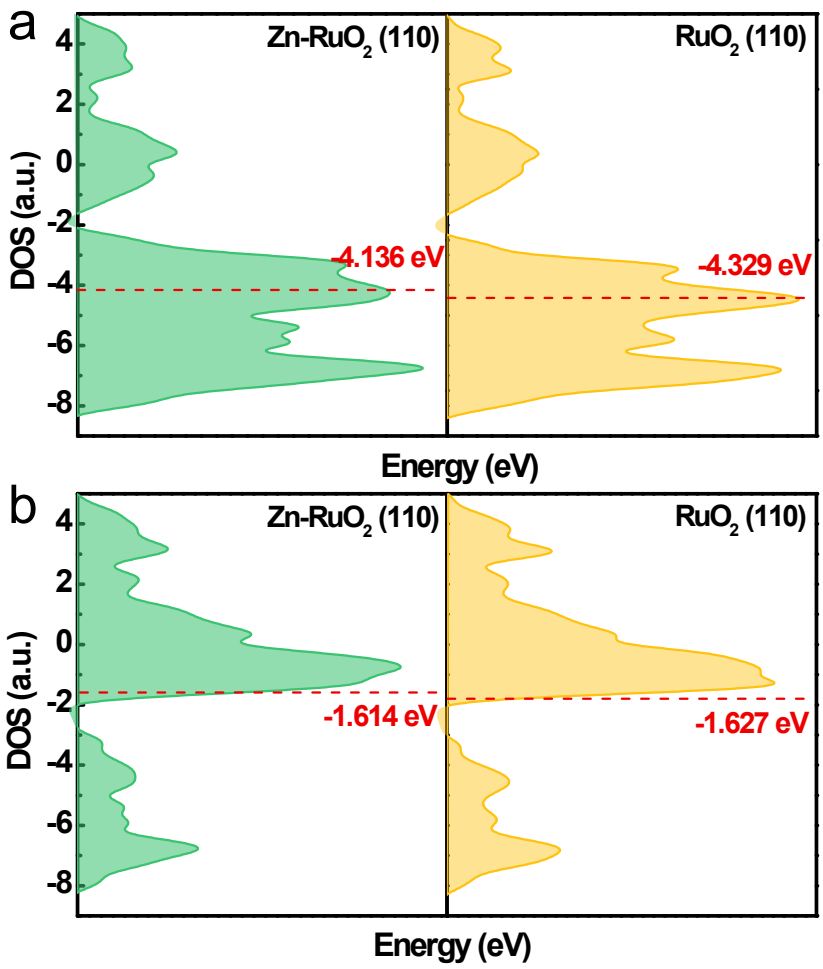

Fig. S19. P-band and d-band center level of RuO_2 (110) and Zn-RuO_2 (110).

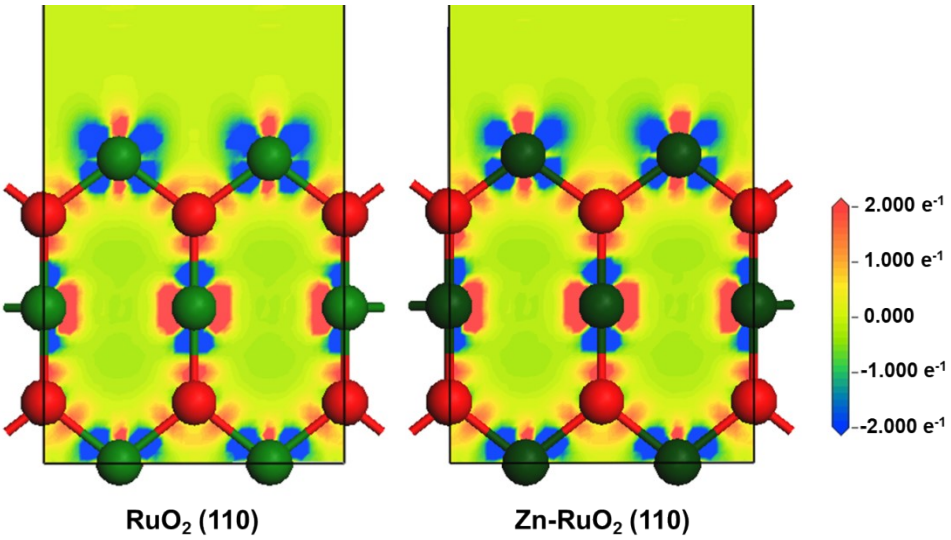

Fig. S20. Electron density difference of RuO_2 (110) and Zn-RuO_2 (110).

Table S1. The Ru, Zn and O element contents in Zn-RuO_2, E-Zn-RuO_2, C-Zn-RuO_2 and E-C-Zn-RuO_2 samples.

	Zn-RuO_2	**E-Zn-RuO_2**	**C-Zn-RuO_2**	**E-C-Zn-RuO_2**	**E-Zn-RuO_2 after OER**
Ru	12.33	18.46	8.49	6.31	15.96
Zn	21.14	1.38	1.51	0.89	1.83
O	66.53	80.46	90.00	92.8	82.22

Table S2. The relative ratio of surface Ru(0) and Ru(IV) in RuO_2, Zn-RuO_2, E-Zn-RuO_2, C-Zn-RuO_2 by Ru 3*p* XPS fitting.

	RuO_2	**Zn-RuO_2**	**E-Zn-RuO_2**	**C-Zn-RuO_2**
The ratio of Ru^0/Ru^{4+}	0.4631	0.5654	0.2805	0.6027

Table S3. Comparison of OER performance in acidic media of E-Zn-RuO_2 with previously reported RuO_2-based catalysts. (η is the overpotential at 10 mA cm^{-2}, mV. b is Tafel slope, mV dec^{-1}.)

Catalysts	Media	η	b	Reference
E-Zn-RuO_2	0.5 M H_2SO_4	178	50.9	**This work**
Cu-RuO_2	0.5 M H_2SO_4	188	44.0	**[5]**
Zn-RuO_2	0.5 M H_2SO_4	206	49.2	**[6]**
Cu-RuO_2-300	0.5 M H_2SO_4	201	55	**[7]**
0.27-RuO_2@C	0.5 M H_2SO_4	250	66	**[8]**
IrO_2-RuO_2@Ru	0.5 M H_2SO_4	281	55	**[9]**
RuO_2-$NaPO_3$	0.5 M H_2SO_4	250	110	**[10]**
RuO_2	0.5 M H_2SO_4	219	44.9	**[11]**
$RuNi_2$@G-250	0.5 M H_2SO_4	227	65	**[12]**
RuO_2 NSs	0.5 M H_2SO_4	199	38.2	**[13]**
IrO_2-RuO_2/C	0.5 M H_2SO_4	188	42	**[14]**
1D-RuO_2-CN_x	0.5 M H_2SO_4	250	52	**[15]**
RuO_2/$(Co,Mn)_3O_4$	0.5 M H_2SO_4	270	77.0	**[16]**
$Co_{0.11}Ru_{0.89}O_{2-\delta}$ (350)	0.5 M H_2SO_4	169	47	**[17]**
IrO_2@RuO_2	0.5 M H_2SO_4	270	60	**[18]**
S-$RuFeO_x$	0.1 M $HClO_4$	187	40	**[19]**
Macro-RuO_2	0.5 M H_2SO_4	263	49	**[20]**

Table S4. Bader charge analysis of pure Zn-RuO_2 (110).

Table Bader charge analysis of Zn-RuO_2 (110).			
Atom	**Charge**	**Atom**	**Charge**
O1	6.58	O17	6.50
O2	6.54	O18	6.51
O3	6.60	O19	6.51
O4	6.58	O20	6.50
O5	6.54	Zn1	11.05
O6	6.60	Ru1	15.30
O7	6.50	Ru2	14.92
O8	6.51	Ru3	15.25
O9	6.51	Ru4	15.06
O10	6.50	Ru5	14.91
O11	6.58	Ru6	15.07
O12	6.54	Ru7	15.30
O13	6.60	Ru8	14.92
O14	6.58	Ru9	15.25
O15	6.54	Ru10	15.07
O16	6.50	Ru11	15.07

Table S5. Bader charge analysis of pure RuO_2 (110).

Table Bader charge analysis of RuO_2 (110).			
Atom	**Charge**	**Atom**	**Charge**
O1	6.58	O17	6.50
O2	6.54	O18	6.64
O3	6.64	O19	6.51
O4	6.58	O20	6.53
O5	6.54	Ru1	15.30
O6	6.64	Ru2	14.92
O7	6.50	Ru3	15.18
O8	6.51	Ru4	15.07
O9	6.51	Ru5	14.92
O10	6.49	Ru6	14.95
O11	6.58	Ru7	15.30
O12	6.54	Ru8	14.92
O13	6.54	Ru9	15.18
O14	6.58	Ru10	15.06
O15	6.54	Ru11	14.90
O16	6.64	Ru12	14.92

Table S6. Gibbs free energy of every intermediate during the OER process for RuO_2 (110) and Zn-RuO_2 (110).

	ΔG(*H_2O)	**ΔG(*OH)**	**ΔG(*O)**	**ΔG(*OOH)**	**ΔG(*OO)**	**ΔG(O_2)**
RuO_2 (110)	-0.64	1.59	0.94	1.54	-0.308	1.80
Zn-RuO_2 (110)	-0.42	1.41	1.05	1.34	-0.11	1.95

Reference

1 J. P. Perdew, M. Ernzerhof and K. Burke, *J. Chem. Phys.*, 1996, **105**, 9982−9985.

2 G. Kresse and D. Joubert, *Phys. Rev. B*, 1999, **59**, 1758−1775.

3 S. Chen, H. Huang, P. Jiang, K. Yang, J.F. Diao, S.P. Gong, S. Liu, M.X. Huang, H. Wang and Q.W. Chen, *ACS Catal.*, 2020, **10**, 1152−1160.

4 R.R. Rao, M.J. Kolb, N.B. Halck, A.F. Pedersen, A. Mehta, H. You, K.A. Stoerzinger, Z.X. Feng, H.A. Hansen, H. Zhou, L. Giordano, J. Rossmeisl, T. Vegge, I. Chorkendorff, I.E.L. Stephens and Y. Shao-Horn, *Energy Environ. Sci.*, 2017, **10**, 2626.

5 J.W. Su, R.X. Ge, K.M. Jiang, Y. Dong, F. Hao, Z.Q. Tian, G.X. Chen and L. Chen, *Adv. Mater.*, 2018, **30**, e1801351.

6 H. Zhang, B. Wu, J.W. Su, K.Y. Zhao and L. Chen, *ChemNanoMat*, 2021, **7**, 117−121.

7 Y.-Y. Feng, S. Si, G. Deng, Z.-X. Xu, Z. Pu, H.-S. Hu, C.-B. Wang, *J. Alloys Compd.*, 2022, **892**, 162113.

8 H.-S. Park, J.C. Yang, M.K. Cho, Y. Lee, S. Cho, S.-D. Yim, B.-S. Kim, J.H. Jang and H.-K. Song, *Nano Energy*, 2019, **55**, 49−58.

9 J.Q. Shan, C.X. Guo, Y.H. Zhu, S.M. Chen, L. Song, M. Jaroniec, Y. Zheng and S.-Z. Qiao, *Chem*, 2019, **5**, 445−459.

10 S. Anantharaj and S. Kundu, *Curr. Nanosci.*, 2017, **13**, 333−341.

11 Z.P. Wang, B.B. Xiao, Z.P. Lin, S.J. Shen, A.J. Xu, Z.X. Du, Y.C. Chen and W.W. Zhong, *J. Energy Chem.*, 2021, **54**, 510−518.

12 X.J. Cui, P.J. Ren, C. Ma, J. Zhao, R.X. Chen, S.M. Chen, N P. Rajan, H.B. Li, L. Yu, Z.Q. Tian and D.H. Deng, *Adv. Mater.*, 2020, **32**, 1908126.

13 Z.L. Zhao, Q. Wang, X. Huang, Q. Feng, S. Gu, Z. Zhang, H. Xu, L. Zeng, M. Gu and H. Li, *Energy Environ. Sci.*, 2020, **13**, 5143−5151.

14 R. Samanta, P. Panda, R. Mishra and S. Barman, *Energy Fuels*, 2022, **36**, 1015−1026.

15 T. Bhowmik, M.K. Kundu, S. Barman, T. Bhowmik, M.K. Kundu and S. Barman, *ACS Appl. Mater. Interfaces*, 2016, **8**, 28678−28688.

16 S.Q. Niu, X.-P. Kong, S.W. Li, Y.Y. Zhang, J. Wu, W.W. Zhao and P. Xu, *Appl. Catal. B Environ.*, 2021, **297**, 120442.

17 Y.Y. Tian, S. Wang, E. Velasco, Y.P. Yang, L.J. Cao, L.J. Zhang, X. Li, Y.C. Lin, Q.J. Zhang and L. Chen, *iScience*, 2020, **23**, 100756.

18 T. Audichon, T.W. Napporn, C. Canaff, C. Morais, C. Comminges and K.B. Kokoh, *J. Phys. Chem. C*, 2016, **120**, 2562−2573.

19 Y.R. Xue, J.J. Fang, X.D. Wang, Z.Y. Xu, Y.F. Zhang, Q.Q. Lv, M.Y. Liu, W. Zhu and Z.B. Zhuang, *Adv. Funct. Mater.*, 2021, **31**, 2101405.

20 C. Baik, S.W. Lee and C. Pak, *Micropor. Mesopor. Mater.*, 2020, **309**, 110567.